

Cryptic Magma Chamber in the Deccan Traps imaged using receiver function

Gokul Saha¹, Vivek Kumar², Dipak Kumar Chaubey², and Shyam S Rai³

¹Indian Institute of Science Education and Research, Pune

²Indian Institute of Science Education and Research Pune

³Indian Institute of Science Education and Research

January 3, 2023

Abstract

We present the first evidence for a lower S-wave velocity ($V_s \sim 3.3$ to 3.5 km/s) at 8-17 km depth underlying a 4 km thick high-velocity zone with $V_s > 3.8$ km/s beneath the west coast and the neighbouring parts of the Deccan Volcanic Province, India, coinciding with the last phase of volcanism. The velocity structure is derived from joint inversion of receiver function from 9 seismographs operated along ~ 106 km long W-E profile with the surface wave dispersion data. The low-velocity layer possibly represents the horizontally elongated frozen magma reservoir, the source for the magma eruption at ~ 65 million years produced due to the interaction of the Reunion hotspot with India. The shallow, high-velocity layer could be basaltic mafic intrusions responsible for the production of massive CO₂ degassing. The Moho deepens beneath the west coast to ~ 45 km due to 10-15 km of underplating as a consequence of magma upwelling.

Hosted file

951628_0_art_file_10515058_rm9979.docx available at <https://authorea.com/users/564423/articles/611247-cryptic-magma-chamber-in-the-deccan-traps-imaged-using-receiver-function>

Hosted file

951628_0_supp_10514966_rm1n6d.docx available at <https://authorea.com/users/564423/articles/611247-cryptic-magma-chamber-in-the-deccan-traps-imaged-using-receiver-function>

14 **Abstract**

15 We present the first evidence for a lower S-wave velocity ($V_s \sim 3.3$ to 3.5 km/s) at 8-
16 17 km depth underlying a 4 km thick high-velocity zone with $V_s > 3.8$ km/s beneath the west
17 coast and the neighbouring parts of the Deccan Volcanic Province, India, coinciding with the
18 last phase of volcanism. The velocity structure is derived from joint inversion of receiver
19 function from 9 seismographs operated along ~ 106 km long W-E profile with the surface
20 wave dispersion data. The low-velocity layer possibly represents the horizontally elongated
21 frozen magma reservoir, the source for the magma eruption at ~ 65 million years produced
22 due to the interaction of the Reunion hotspot with India. The shallow, high-velocity layer
23 could be basaltic mafic intrusions responsible for the production of massive CO_2 degassing.
24 The Moho deepens beneath the west coast to ~ 45 km due to 10-15 km of underplating as a
25 consequence of magma upwelling.

26 **Plain language summary**

27 The Deccan Traps, in western India, is a continental flood basalt province. The
28 volcanism occurred around 65 million years (Ma) ago when India was in the southern
29 latitude. While moving northward, India interacted with the Reunion hotspot, leading to
30 increased mantle temperature and consequent melting. Due to buoyancy, the magma moved
31 upward and ponded towards the crust-mantle boundary. When the magma in these lower
32 crustal or Moho-depth chambers is buoyant and overpressures are high enough to cause the
33 overlying crust to fail, it will ascend via dikes and assimilate into a shallow crust. The
34 process is expected to produce significant crustal modification due to increased heat transfer
35 from the mantle to the surface and chemical transformation. Existing geophysical knowledge
36 of the Deccan traps does not provide evidence for such crustal transformations. Using data
37 from a high-density seismic experiment to construct a detailed model of the crust, we
38 discovered magma ponding at the crust-mantle boundary beneath the coastal basin, an
39 extensive low-velocity layer in the upper/mid crust possibly representing the horizontally
40 elongated frozen magma reservoir, and a densified high-velocity layer in the shallow crust (at
41 a depth of 4-8 km) representing basaltic mafic intrusions.

42 **1.0 Introduction**

43 Understanding the location and form of magma storage in the crust is important to
44 model fundamental Earth processes such as crustal growth, ore deposit formation, and
45 predicting geohazards related to volcanism (Hill et al., 1991; Richards et al., 1989; Self et al.,

46 2008). The generation of magma requires two operations: the partial melting of rocks, either
47 by supplying heat or by reducing the pressure and consequently changing the solidus
48 temperature; and the melt separation from the residual solid matrix through relative motion
49 between the matrix and the melt (McKenzie, 1984). The conceptual model for continental
50 flood basalt, first proposed by Cox (1980), includes magma's origin in the mantle, most
51 likely due to the interaction of mantle plumes at the base of the lithosphere, followed by the
52 melt rising towards the base of the crust, where rheological and density contrasts may cause
53 the melt to pond and form large primitive magma chambers (Ridley & Richards, 2010).
54 When the magma in these chambers at lower crust or Moho depth is buoyant and
55 overpressures are high enough to cause the failure of the overlying crust, it will ascend via
56 dikes and assimilate at a shallow crustal depth (e.g., Bachmann & Huber, 2016; Black et al.,
57 2021; Sparks et al., 1984).

58 Geophysical techniques have been successfully used in investigating the structure of
59 the magma plumbing in active volcanic systems (e.g., Chrapkiewicz et al., 2022; Jaxybulatov
60 et al., 2014; Lees, 2007; Paulatto et al., 2022; Peng & Humphreys, 1998; Ward et al., 2014).
61 This knowledge helps in providing critical insights into magma emplacement, mush
62 evolution, and modelling the quantum of CO₂ outflux (e.g., Cartwright & Hansen, 2006;
63 Kasbohm, 2022; Muirhead et al., 2014; Tian & Buck, 2022). Geophysical imaging of old
64 volcanic systems like the Deccan, Columbia, and Siberia is, however, more difficult and
65 debated due to weak geophysical signatures as a consequence of magma solidification
66 because of heat loss.

67 The Deccan Volcanic Province (DVP) is a Large Igneous Province (LIP)
68 encompassing an area of about a half-million km² in west-central India (Figure 1a), with a
69 possible extension of an additional one million km² beneath the Arabian Sea to the west
70 (Colleps et al., 2021; Jay & Widdowson, 2008; Sen, 2001). The volcanism in DVP was the
71 consequence of the interaction of the fast-moving Indian plate with the Reunion mantle
72 plume in the southern latitude at around 65 Ma (Mahoney, 1988; Morgan, 1972). The basalt
73 attains a maximum thickness of 1.5-2 km along the Western Ghat escarpment (Holmes, 1965)
74 and thins eastward. To the west of the escarpment is the narrow, flat coastal plain that is
75 divided by an N-S extensional fault referred to as the Panvel Flexure (Figure 1b). The nature
76 and genesis of the Panvel Flexure are debated (Dessai & Bertrand, 1995). The DVP is one of
77 the most interesting subjects of research for three principal reasons: its enormous size, a

78 typical area to understand the process of magmatism in the planetary system, and a unique
 79 case for solid earth-climate interaction leading to major mass extinction and rapid climate
 80 change. A series of recent papers (e.g., Krishnamurthy et al., 2000; Mittal et al., 2021; Nava
 81 et al., 2021; Self et al., 2022) provide a detailed review of the subject.
 82

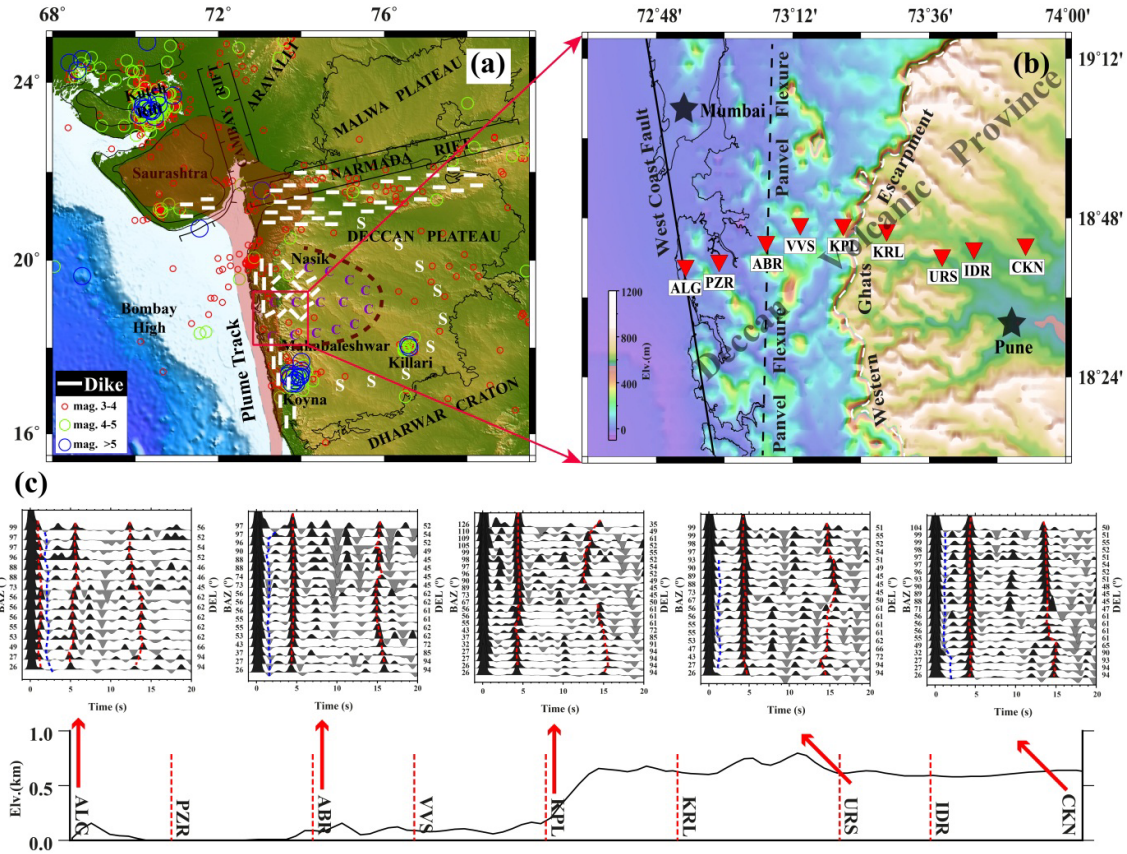


Figure 1. Map of the study area and the data set used. (a) A topographic map of the DVP and surrounding area. Local seismicity is shown in circles. The pink shade along the west coast represents the mantle plume track. White dashed lines indicate dikes. The area marked as “C” indicates compound magma flow, and that marked as “S” indicates simple flow (Sen, 2001; Sen & Chandrasekharam, 2011). (b) Location of broadband seismological stations operated during 2020-21, along with important tectonic features. (c) A plot of selected RFs with varying earthquake distance and back azimuth for selected stations.

83 Numerous geophysical experiments have been performed over the DVP to investigate
 84 its crustal structure. None of them, however, show evidence of an upper-crustal magma
 85 chamber beneath it (e.g., Bhattacharji et al., 2004; Chopra et al., 2014; Kaila et al., 1981;

86 Krishna et al., 1991; Mohan & Kumar, 2004; Patro & Sarma, 2016; Patro et al., 2018; Prasad
87 et al., 2018; Tiwari et al., 2001). Some of these studies do indicate the presence of magma
88 underplating, albeit with poorly quantified thickness, location, velocity, and density. We
89 present here the first evidence and location of the possible magma ponding in the lower crust,
90 and the shallow magma chamber through seismic imaging of the crust beneath the western
91 segment of the DVP adjoining the west coast of India using broadband seismic waveform
92 data (Figure 1b). Our inference is based on the joint inversion of receiver function and
93 surface wave dispersion data (Julia et al., 2000), supported by the modelling of ambient noise
94 data (e.g., Shapiro et al., 2005).

95 **2.0 Data and preliminary analysis**

96 We deployed 9 broadband seismographs (Figure 1b) aligned W-E from the west coast
97 of India, between January 2020 and September 2021, with an inter-station spacing of 10-15
98 km. The experiment was executed in the region of the final Deccan eruption, where the
99 magma chamber is hypothesized based on the analysis of megacrysts in the Giant Plagioclase
100 Basalts (Higgins & Chandrasekharam, 2007). The region has a large number of dikes and
101 compound magma flows (Figure 1a). The P receiver functions (RFs) were computed for
102 selected earthquakes of magnitudes above 5.5 and epicenter distances between 30° and 95°
103 (Figure S1 a, b) using a time domain iterative deconvolution approach (Ligorria & Ammon,
104 1999). A low-pass Gaussian filter was applied with a parameter of 2.5, which means the
105 corresponding cut-off frequency is ~ 1.2 Hz and the pulse width of ~ 1.0 s. These RFs were
106 used to compute the structural model using Common Conversion Point (CCP) migration
107 (Ducker & Sheehan, 1997) and perform inversion jointly with Rayleigh wave group velocity
108 dispersion (e.g., Julia et al., 2000).

109 A sample of RFs at a few locations is presented in Figure 1c. Important features of the
110 RFs are a positive conversion at about ~ 0.5 s, a negative one at ~ 1.5 s, and a Moho converted
111 phase at 4.5-5.5 s. To analyse the shallow depth conversions in detail, we computed RF at a
112 location for varying Gaussian widths from 2.5 to 15, corresponding to a maximum frequency
113 content of 1.2 Hz to 6 Hz (Figure S1c). Here, the P phase arrival (L1) is delayed by 0.1 s
114 which suggests the presence of a thin low-velocity layer possibly due to the Deccan basalt
115 with Vs of 1.8-2.4 km/s and a thickness of about 1 km (Ray et al., 2021). A positive P-S
116 conversion at 0.6 s (L2) represents a 4-5 km thick high-velocity layer. Further, a low-velocity
117 layer (LVL) in the upper crust is identified by two P-to-S converted phases at 1.4 s and 1.7 s
118 (L3 & L4) due to the conversion from the top and bottom of the LVL. The approximate

119 location of the LVL is between 10 and 16 km. The Moho converted phase is identified at
120 about 4.5 s (marked as M), corresponding to a depth of about 36 km. A plot of the RFs time
121 series along the profile for an earthquake (Figure S1d) shows the presence of these features,
122 albeit with local variations in layer depth and velocity contrast. The RFs along the profile
123 show the delayed arrival time of the Moho conversion with a reduced amplitude below the
124 coastal stations, particularly the two westernmost stations. To quantify these parameters, we
125 modelled receiver function data, as discussed in subsequent sections.

126 **3.0 Methodology and result**

127 3.1 Joint inversion of receiver function and surface wave data

128 To map the interface depth and provide a reliable velocity image, we perform an
129 inversion of the RF time series with the surface wave dispersion data (e.g., Julia et al., 2000)
130 using an iterative sequence of linearized least squares inversions (Herrmann & Ammon,
131 2002). Details of the methodology are provided in Supplementary Text S1. The velocity
132 model at individual stations presented in Figures S2 and S3 is interpolated to generate a W-E
133 velocity profile to a depth of 60 km (Figure 2a). The Moho is identified by depth to
134 maximum velocity gradients beyond the depth of 30 km and velocity beyond V_s of 4.3 km/s,
135 corresponding to a typical peridotite P-velocity of >7.6 km/s. The Moho depth varies from 37
136 to 40 km, except in the coastal region, where it increases to about 45 km. Similar Moho
137 depths are obtained using H-K stacking as well (Figure S4). A thick (10-15 km) underplated
138 layer (UL) with $V_s >4.0$ km/s above the deeper part of Moho is mapped beneath the west
139 coast, compared with 3-5 km thickness elsewhere. A high-velocity layer (HVL) of V_s 3.7-3.9
140 km/s is identified in the shallower part (4-8 km) lying over the prominent low-velocity layer
141 (LVL) in the depth range of 8 to 17 km with V_s of 3.3-3.5 km/s.

142 We performed a number of forward models to ascertain the robustness of the Moho
143 depth, the high-velocity underplating layer, and low and high velocities in the shallower crust
144 (Figure S5 a-d). To examine the continuity of the LVL in other parts of the DVP, we
145 modelled data from regionally distributed stations (Figure S6). The result shows no evidence
146 for such an LVL away from the study region. In the absence of a well-distributed network,
147 we are unable to delineate the zone with the LVL in the shallow crust.

148 3.2 Receiver function imaging

149 We create a depth image of impedance contrast below the profile using the Common
150 Conversion Point (CCP) stacking method (Dueker & Sheehan, 1997). The CCP stacks are
151 constructed by back-projecting each RF time series to its appropriate spatial location in depth
152 using ray theory and a shear wave velocity model (and a V_p/V_s of 1.74) derived from a joint
153 inversion for the easternmost station, CKN (Figure 1b). The spatial location of the converted
154 phase at depths of 10, 30, and 50 km is presented in Figure S7. To successfully image
155 structure that varies along the section, the Fresnel zones must overlap by ~50% or more at the
156 depth of interest (Zhai & Levander, 2011). The Fresnel zone width for Ps at 10, 30, and 50
157 km depth is ~4, 6, and 12 km. The RF stack is computed in a bin of 5 km width and every 1
158 km depth and further smoothed over 10 km horizontal window. The CCP image coherently
159 stacks RF phase conversions and also partially cancels random noise. The CCP image (Figure
160 2b) reveals three characteristic features: a positive conversion (HVL) at about 5 km,
161 underlain by a negative conversion (LVL) at ~10 km, and the Moho depth of 35-40 km that
162 increases to ~45 km below the coastal plain. The Moho depth, determined using H-K
163 stacking (Figure S4), is superimposed on the CCP image (Figure 2b). Three different
164 approaches: joint inversion of RF and surface waves, CCP migration, and H-K stacking show
165 very similar and consistent features.

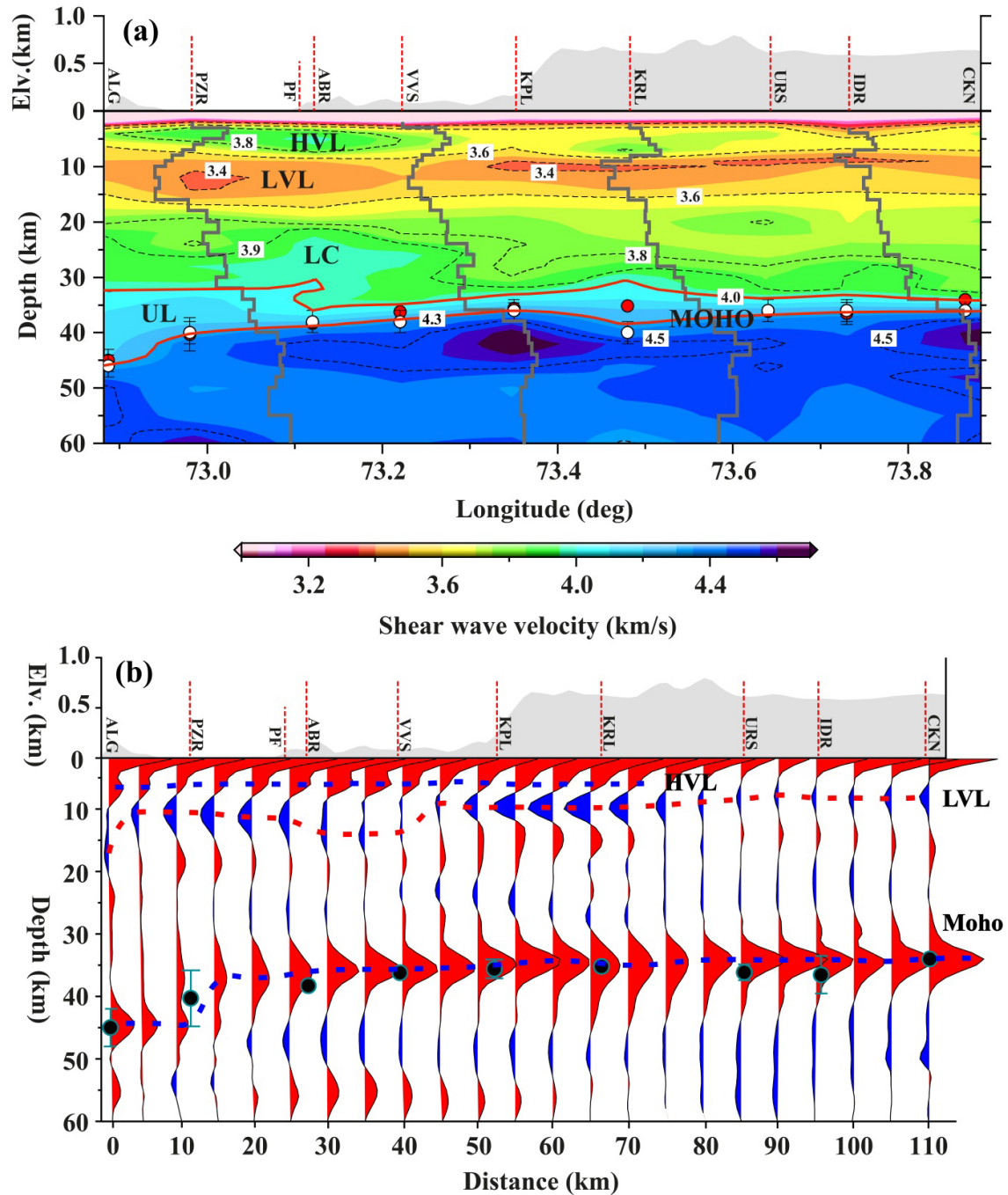


Figure 2. (a) Shear wave velocity profile created through the joint inversion of RF and surface wave dispersion data. Grey lines are 1D velocity models at selected stations. Red circles indicate the Moho from H-K stacking method (Figure S4) and the white circles are the Moho from joint inversion (Figure S3). HVL-High velocity layer, LVL-Low velocity layer, LC-Lower crust ($V_s > 3.8-4.0$ km/s), UL-Underplated layer ($V_s > 4.0$ km/s), PF-Panvel

Flexure. (b) CCP image along the seismic profile. Black circles are the Moho estimates from H-K stacking (Figure S4).

166 **4.0 Discussion**

167 A velocity-depth section of the crust along a ~106 km long profile from the west coast
168 of the DVP in west-central India is presented in Figure 2a. We examine the possible
169 alteration in Pre-Deccan crust in Figure 3a due to the volcanism. Deep drill hole samples
170 from the Koyna region, about 100 km south of this profile, show that the basement of the
171 DVP closely resembles the Dharwar craton (Ray et al, 2021; Shukla et al., 2022). An
172 ensemble of velocity models (Figure 3a) of the DVP along the profile, compared with the
173 Dharwar craton (Borah et al., 2014; Chaubey et al., 2022), suggests significant differences
174 between the crustal properties: a lower velocity at a depth of 8-17 km and a higher velocity at
175 4-8 km below the seismic profile in the DVP. We observe a laterally variable underplated
176 basal layer ($V_s > 4.0$ km/s) in the lower crust. The Moho depth is mapped at ~35 km along the
177 profile, except beneath the west coast over a distance of 40 km, where it deepens to ~45 km.
178 The deep Moho zone beneath the coastal plain coincides with significant magma
179 underplating of ~10-15 km and terminates in the east below the Panvel Flexure. We discuss
180 the significance of these features below.

181 4.1 The lower crust and uppermost mantle

182 The Deccan magmas were produced by high-temperature melting at a depth of 60-100
183 km (Sen, 2001), located beneath the west coast of India and underlying regions of uplift in
184 dynamic topography (Glišović & Forte, 2017). Existing seismological observations are
185 inadequate to define the spatial extent of high mantle temperatures. Iyer et al. (1989), based
186 on travel-time modelling of teleseismic rays, proposed that most of the DVP is underlain by a
187 thick continental root, except for the westernmost part adjoining the west coast. Being at the
188 edge of the craton, this segment of the DVP has thin lithosphere and was most influenced by
189 the Réunion hot spots (Sharma et al., 2018). The mantle melting led to magma ponding at the
190 base of the crust, which eventually resulted in high-velocity underplating and crustal
191 thickening as observed in the coastal plain. The Moho is about 10-15 km thicker beneath the
192 west coast due to the presence of an underplated layer with $V_s > 4.0$ km/s (Figure 2a), as
193 expected from the presence of solidified olivine and clinopyroxene rich cumulates in deep
194 magma reservoirs (Cox, 1993). Interestingly, we don't observe magma underplating to the
195 east of the western Ghat (about 60 km from the coast), which correlates well with

196 seismological evidence for undisturbed lithospheric mantle in the DVP to the east of the
 197 western Ghat (Iyer et al., 1989; Kumar & Mohan, 2005).

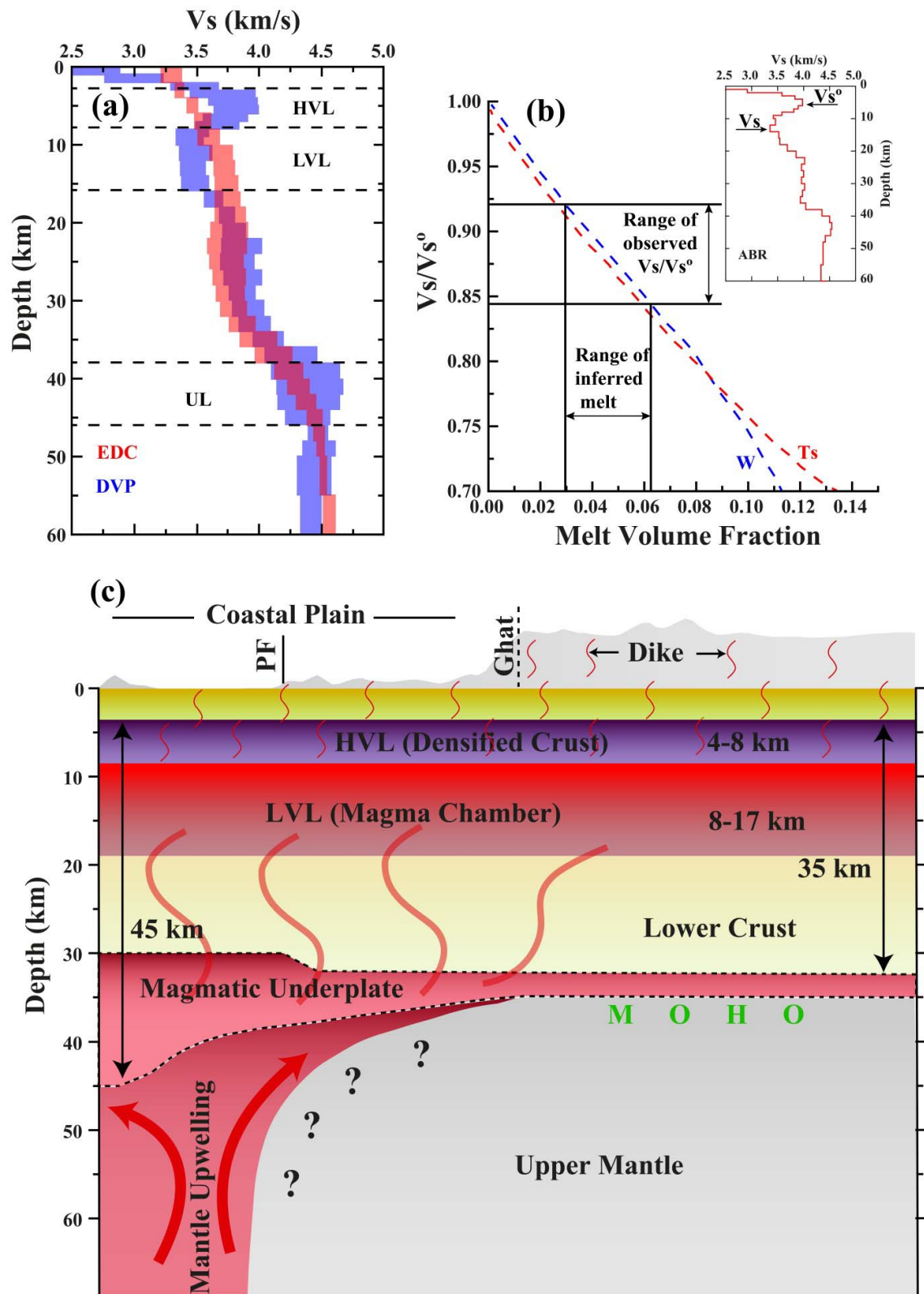


Figure 3. (a) Plot of an ensemble of velocity models for seismic stations located in the DVP and Dharwar craton. HVL-High velocity layer, LVL-Low velocity layer, UL-Underplated layer. (b) Proportional velocity reduction (V_s/V_s°) versus melt volume fraction. Horizontal lines indicate proportional velocity reductions in the low-velocity layer (LVL) for the regions. W: blue line is an analytical relationship of Watanabe (1993) for randomly oriented triangular melt tubes. Ts: Red dashed line is an analytical relationship of Taylor and Singh (2002) for the slow propagation direction in a medium containing perfectly aligned oblate spheroids of aspect ratio 10. (c) Schematic view of the magmatic system beneath the DVP coinciding with seismic profile in Figure 1b. The thick red arrow indicates the ascending direction of the melts from the upper mantle to the crust-mantle boundary. PF is Panvel Flexure.

198 4.2 Low velocity in upper crust

199 At a depth of 8 to 17 km, we observe an approximately 0.1-0.4 km/s (or 3-12%)
 200 velocity reduction ($V_s \sim 3.3-3.5$ km/s) relative to the Dharwar Craton ($V_s \sim 3.7$ km/s). Such
 201 low velocity in the shallow crust has been reported in various geological settings as a
 202 consequence of crustal rejuvenation in cratonic regions, partial melting, felsic composition,
 203 or strong radial anisotropy (Beck & Zandt, 2002; Diaferia & Cammarano, 2017; Gao et al.,
 204 2020; Kind et al., 1996; Li et al., 2003; Ward et al., 2014; Zheng et al., 2015; Zorin et al.,
 205 2003).

206 A global compilation of experimentally measured shear wave velocities of dry rocks
 207 (Christensen, 1996) at room temperature and lithostatic pressure of 400 MPa, corresponding
 208 to a depth of about 12 km, suggests only a few rocks like Andesite ($V_s \sim 3.1$ km/s); Basalt
 209 ($V_s \sim 3.3$ km/s); Slate ($V_s \sim 3.3$ km/s); Phyllite ($V_s \sim 3.5$ km/s); Granite Gneiss ($V_s \sim 3.6$ km/s)
 210 fall in the observed velocity range. To extrapolate these velocities to mid-crustal
 211 temperatures, we used a V_s decrease of $0.2 \text{ m/s}/^\circ\text{C}$, an average value determined from a range
 212 of gneisses (Kern et al., 2001). Heat flow estimates in the neighbouring Koyna region (Figure
 213 1a) from a 1,500 m deep borehole yielded an average value of 45 mW/m^2 (Ray et al., 2021).
 214 Deep drilling confirms that the Deccan trap is underlain by granitoid rocks (TTG). Their 1-D
 215 steady-state thermal modelling indicates temperatures could vary from 165°C to 250°C at 10
 216 km depth, much higher than previously reported. These results depend on the assumed
 217 thermal conductivity of the underlying rock and should be used cautiously. Therefore,
 218 although higher temperature is possibly a contributing factor, it may not be the only cause of
 219 the observed low upper-crustal velocity.

220 The LVL could also be due to the presence of partial melts, aqueous fluids, or both
221 since these are easily capable of a velocity decrease of 7–17% (Takei, 2000; Watanabe,
222 1993). To constrain the percentage of melt present in the DVP, we compared our shear-wave
223 velocities with theoretical and experimentally-derived relationships between V_s and melt
224 percentage (Figure 3b). We used the ratio of V_s to V_s° , which represents the minimum of the
225 LVL and the upper-crustal peak velocity, respectively, for the velocity profile at each station
226 (Figure 2a). Using Figure 3b, we obtain the presence of a moderate to low melt percentage
227 (3-6%) corresponding to the LVL. In a detailed thermodynamic model considering anhydrous
228 and two wet components, Diaferia and Cammarano (2017) inferred that the V_s at 400 MPa is
229 influenced more by the presence of melt compared to water. They concluded that $V_s < 3.6$
230 km/s in the crystalline crust would imply a strong contribution of sediment and/or melt.
231 Additionally, deep magmas were transported upward through the crust via the development
232 and propagation of faults (Downs et al., 2018), and some liquid and/or gas could have
233 migrated into these faults, changing the physical properties of the nearby rocks. Thus, partial
234 melt and fluid-filled faults are significant causes for producing the crustal low-velocity zone
235 below magmatic provinces.

236 The other factor influencing shear wave velocity is the seismic anisotropy in the
237 Earth's crust, observed in almost all geological and tectonic settings (e.g., Illsley-Kemp et al.,
238 2021; Johnson et al., 2011; Li & Peng, 2017; Savage et al., 2017). It is caused by structural
239 features such as faults (Zinke & Zoback, 2000), and aligned melt pockets (e.g., Bastow et al.,
240 2010; Dunn et al., 2005; Keir et al., 2005, 2011), where the polarization direction is parallel
241 to the trend of structural features. In the upper crystalline crust, where anisotropy is generally
242 weak, it is explained by micro-cracking often related to present day stress and also mineral
243 fabric. In the middle and lower crust, it is generally attributed to rock texture, like mineral
244 alignment from sheared and metamorphosed rock. Mahan (2006) argued that deformed
245 granitic rocks may also have a significant increase in mica content due to the breakdown of
246 feldspar or fluid related mass transfer and can have significant anisotropy. Seismic anisotropy
247 has been inferred in dikes or sill complexes where fine-scale layering affects the macro-
248 mechanical properties of the crustal material. Tectonically active regions (Shapiro et al.,
249 2004; Moschetti et al., 2010), and volcanic regions (Jaxybulatov et al., 2014) show well
250 defined anisotropy related to the horizontal layering associated with mineralogical
251 preferential orientation. We present here the first report of crustal anisotropy using limited
252 data.

253 Simultaneous inversion of the dispersion curves of Rayleigh and Love surface waves
254 has been widely used to estimate radial anisotropy in the crust using dispersion measurements
255 at periods <20 s, which is possible with the correlation of the ambient seismic noise field
256 (Shapiro et al., 2005). Following this approach, Das and Rai (2017) inferred 3% anisotropy in
257 the upper and middle crust of the Dharwar craton. Due to the short length of the present
258 profile, we could only retrieve Rayleigh and Love wave phase velocity dispersion data up to
259 20 s through cross-correlation of the ambient noise field only for two inter-station pairs
260 (Figure S8a). An inversion of dispersion data for these two pairs (Figures S8 b, c) shows the
261 presence of positive radial anisotropy ($V_{sh} > V_{sv}$) in the depth of 8-17 km, where the low
262 velocity is inferred. The magnitude of the anisotropy ranges from 5-15%, indicating the
263 possible contribution of mineral alignment in the horizontal directions during the magma
264 flow, leading to V_s reductions in the LVL layer as discussed earlier.

265 4.3 High velocity in the shallow crust

266 Our velocity model shows the presence of shear velocities of 3.7-3.9 km/s in the depth
267 range of 4-8 km, in contrast with the 3.5 km/s observed over the Dharwar craton, which is
268 higher by 0.2-0.4 km/s (5-10%). The first observation of such a high velocity upper crust in
269 DVP was made by Rai et al. (1999) using local earthquake tomography in the neighbouring
270 Koyna region. The high velocity at shallow depths is at odds with the general understanding
271 of continental crust composition, where density generally increases with depth. Assuming a
272 shear velocity-density relation (Brocher, 2005), we infer a high-density layer in the upper
273 crust underlain by a low density one. The denser crust beneath the DVP section is probably
274 due to basaltic crustal intrusions. Tian and Buck (2022) provide a detailed account and
275 reference for extensive mafic intrusion beneath the Columbia River Basalt, Emeishan,
276 Siberian, and Etendeka LIPs, based on geophysical data modelling. They suggest that crustal
277 densification due to voluminous magma intrusion and solidification is necessary for the
278 extrusion of continental flood basalts. Further, crystallization of such pre-eruption intrusions
279 could release enough carbon dioxide to drive substantial global warming before the main
280 phase of flood basalt volcanism. We speculate a similar scenario over the DVP, and the
281 mapped HVL could have been the possible source region for large CO_2 releases.

282 Figure 3c provides a schematic view of the magma plumbing system beneath the DVP
283 as a 2-D W-E oriented cross-section. The mafic magma originates from the upper mantle
284 beneath the west coast and the adjoining sea, ascending in the lower crust to the upper-middle

285 crust. It is ponded at the crust-mantle boundary. A part of the magma intruded into the
286 shallower crust, where it was densified and preserved as a high-velocity layer.

287 **5 Conclusion**

288 We constructed a high resolution crustal velocity model for the ~106 km length of the
289 west-to-east transect, covering part of the Deccan traps from its west coast, using the
290 seismological data at ~10-15 km intervals. We jointly inverted the P-receiver function with
291 surface wave dispersion data. Also, we generated a 1-D velocity anisotropy model to a depth
292 of 25 km from the analysis of two inter-station ambient noise paths. The velocity image
293 provides evidence for a 10-15 km thick high-velocity layer ($V_s > 4.0$ km/s) at the base of the
294 crust, interpreted as a response of dense mafic underplating during magmatism at ~65 Ma and
295 confined to a distance of 40 km only from the coast. In the shallower crust (8-17 km depth), a
296 continuous low-velocity (V_{sv} of 3.3-3.5 km/s) and radially anisotropic ($V_{sh} \sim 4$ km/s) layer is
297 mapped. This low velocity anisotropic layer possibly represents the horizontally elongated
298 frozen magma reservoir, a source for the magma eruption. The low velocity layer underlies a
299 densified high velocity isotropic layer with $V_{sv} > 3.8$ km/s at a depth of 4-8 km, representing
300 basaltic mafic intrusions responsible for the production of massive CO_2 degassing.

301 To improve the magma evolution process beneath the Deccan Volcanic Province,
302 other physical properties of the crust, such as seismic anisotropy, attenuation, temperature,
303 and the V_p/V_s ratio, are needed and are a subject to future investigations.

304 **6 Acknowledgements**

305 We gratefully appreciate the financial support from the Department of Atomic
306 Energy, India in form of a Raja Ramanna Fellowship to SSR and Research Associateship to
307 VK (research grant no. 1003/2021/RRF/R&DII). The field support from Vikrant Bartakke
308 and Vibhas Shevde is greatly appreciated. The Department of Earth & Climate Science,
309 IISER Pune provided generous support towards the field experiment. SSR thanks, Profs.
310 Vinod Gaur, Kanchan Pande, Raymond Duraiswami, and Vivek Kale for many useful
311 discussions on geological aspects of Deccan volcanism and magma plumbing.

312 **7. Data availability statement**

313 Receiver functions, surface wave dispersion, and velocity model at each station are
314 provided as supplementary documents for a peer review process. After acceptance, these data
315 will be made available on a public repository i.e., Zenodo.org.

316 **8. References**

- 317 Bachmann, O., & Huber, C. (2016). Silicic magma reservoirs in the Earth's crust. *American*
318 *Mineralogist*, 101(11), 2377-2404. <https://doi.org/10.2138/am-2016-5675>
- 319 Bastow, I. D., Pilidou, S., Kendall, J. M., & Stuart, G. W. (2010). Melt-induced seismic
320 anisotropy and magma assisted rifting in Ethiopia: Evidence from surface waves.
321 *Geochemistry, Geophysics, Geosystems*, 11(6).
322 <https://doi.org/10.1029/2010GC003036>
- 323 Beck, S. L., & Zandt, G. (2002). The nature of orogenic crust in the central Andes. *Journal of*
324 *Geophysical Research: Solid Earth*, 107(B10), ESE-7.
325 <https://doi.org/10.1029/2000JB000124>
- 326 Bhattacharji, S., Sharma, R., & Chatterjee, N. (2004). Two-and three-dimensional gravity
327 modeling along western continental margin and intraplate Narmada-Tapti rifts: Its
328 relevance to Deccan flood basalt volcanism. *Journal of Earth System Science*, 113(4),
329 771-784. <https://doi.org/10.1007/BF02704036>
- 330 Black, B. A., Karlstrom, L., & Mather, T. A. (2021). The life cycle of large igneous
331 provinces. *Nature Reviews Earth & Environment*, 2(12), 840-857.
332 <https://doi.org/10.1038/s43017-021-00221-4>
- 333 Borah, K., Rai, S. S., Prakasam, K. S., Gupta, S., Priestley, K., & Gaur, V. K. (2014).
334 Seismic imaging of crust beneath the Dharwar Craton, India, from ambient noise and
335 teleseismic receiver function modelling. *Geophysical Journal International*, 197(2),
336 748-767. <https://doi.org/10.1093/gji/ggu075>
- 337 Brocher, T. M. (2005). Empirical relations between elastic wavespeeds and density in the
338 Earth's crust. *Bulletin of the seismological Society of America*, 95(6), 2081-2092.
339 <https://doi.org/10.1785/0120050077>

- 340 Cartwright, J., & Hansen, D. M. (2006). Magma transport through the crust via
341 interconnected sill complexes. *Geology*, *34*(11), 929-932.
342 <https://doi.org/10.1130/G22758A.1>
- 343 Chaubey, D. K., Rai, S. S., Mullick, N., & Das, R. (2022). Unperturbed Archean lithosphere
344 beneath the Eastern Dharwar Craton Kimberlite Field, India: inferred from joint
345 inversion of surface wave dispersion and receiver function data. *Precambrian*
346 *Research (in review)*. <https://doi.org/10.1002/essoar.10512636.1>
- 347 Chopra, S., Chang, T. M., Saikia, S., Yadav, R. B. S., Choudhury, P., & Roy, K. S. (2014).
348 Crustal structure of the Gujarat region, India: New constraints from the analysis of
349 teleseismic receiver functions. *Journal of Asian Earth Sciences*, *96*, 237-254.
350 <https://doi.org/10.1016/j.jseaes.2014.09.023>
- 351 Chrapkiewicz, K., Paulatto, M., Heath, B., Hooft, E., Nomikou, P., Papazachos, C., &
352 Morgan, J. (2022). Magma chamber detected beneath an arc volcano with high-
353 resolution velocity images. *submitted to EarthArXiv*.
354 <https://doi.org/10.31223/X5934R>
- 355 Christensen, N. I. (1996). Poisson's ratio and crustal seismology. *Journal of Geophysical*
356 *Research: Solid Earth*, *101*(B2), 3139-3156. <https://doi.org/10.1029/95JB03446>
- 357 Colleps, C. L., McKenzie, N. R., Guenther, W. R., Sharma, M., Gibson, T. M., & Stockli,
358 D. F. (2021). Apatite (U-Th)/He thermochronometric constraints on the northern
359 extent of the Deccan large igneous province. *Earth and Planetary Science Letters*,
360 *571*, 117087. <https://doi.org/10.1016/j.epsl.2021.117087>
- 361 Cox, K. G. (1980). A model for flood basalt volcanism. *Journal of Petrology*, *21*(4), 629-650.
362 <https://doi.org/10.1093/petrology/21.4.629>
- 363 Cox, S. (1993). Inter-related plutonism and deformation in South Victoria Land, Antarctica.
364 *Geological Magazine*, *130*(1), 1-14. <https://doi.org/10.1017/S0016756800023682>
- 365 Das, R., & Rai, S. S. (2017). Extensive seismic anisotropy in the lower crust of Archean
366 metamorphic terrain, South India, inferred from ambient noise tomography.
367 *Tectonophysics*, *694*, 164-180. <https://doi.org/10.1016/j.tecto.2016.12.002>

- 368 Dessai, A. G., & Bertrand, H. (1995). The “Panvel Flexure” along the Western Indian
369 continental margin: an extensional fault structure related to Deccan magmatism.
370 *Tectonophysics*, 241(1-2), 165-178. [https://doi.org/10.1016/0040-1951\(94\)00077-M](https://doi.org/10.1016/0040-1951(94)00077-M)
- 371 Diaferia, G., & Cammarano, F. (2017). Seismic signature of the continental crust: what
372 thermodynamics says? An example from the Italian Peninsula. *Tectonics*, 36(12),
373 3192-3208. <https://doi.org/10.1002/2016TC004405>
- 374 Downs, D. T., Stelten, M. E., Champion, D. E., Dieterich, H. R., Nawab, Z., Zahran, H., &
375 Shawali, J. (2018). Volcanic history of the northernmost part of the Harrat Rahat
376 volcanic field, Saudi Arabia. *Geosphere*, 14(3), 1253-1282.
377 <https://doi.org/10.1130/GES01625.1>
- 378 Dueker, K. G., & Sheehan, A. F. (1997). Mantle discontinuity structure from midpoint stacks
379 of converted P to S waves across the Yellowstone hotspot track. *Journal of*
380 *Geophysical Research: Solid Earth*, 102(B4), 8313-8327.
381 <https://doi.org/10.1029/96JB03857>
- 382 Dunn, R. A., Lekić, V., Detrick, R. S., & Toomey, D. R. (2005). Three-dimensional seismic
383 structure of the Mid-Atlantic Ridge (35 N): Evidence for focused melt supply and
384 lower crustal dike injection. *Journal of Geophysical Research: Solid Earth*, 110(B9).
385 <https://doi.org/10.1029/2004JB003473>
- 386 Gao, H., Yang, X., Long, M. D., & Aragon, J. C. (2020). Seismic evidence for crustal
387 modification beneath the Hartford rift basin in the northeastern United States.
388 *Geophysical Research Letters*, 47(17), e2020GL089316.
389 <https://doi.org/10.1029/2020GL089316>
- 390 Glišović, P., & Forte, A. M. (2017). On the deep-mantle origin of the Deccan Traps. *Science*,
391 355(6325), 613-616. <https://doi.org/10.1126/science.aah4390>
- 392 Herrmann, R. B., & Ammon, C. J. (2002). Computer programs in seismology: Surface
393 waves, receiver functions and crustal structure. *St. Louis University, St. Louis, MO*,
394 25, 46. <http://www.eas.slu.edu/People/RBHerrmann/CPS330.html>
- 395 Higgins, M. D., & Chandrasekharam, D. (2007). Nature of sub-volcanic magma chambers,
396 Deccan Province, India: evidence from quantitative textural analysis of plagioclase

- 397 megacrysts in the Giant Plagioclase Basalts. *Journal of Petrology*, 48(5), 885-900.
398 <https://doi.org/10.1093/petrology/egm005>
- 399 Hill, R. I., Campbell, I. H., & Griffiths, R. W. (1991). Plume tectonics and the development
400 of stable continental crust. *Exploration Geophysics*, 22(1), 185-188.
401 <https://doi.org/10.1071/EG991185>
- 402 Holmes, A., 1965, Principles of Physical Geology, Thomas Nelson & Sons, London, 1288 p.
- 403 Illsley-Kemp, F., Barker, S. J., Wilson, C. J., Chamberlain, C. J., Hreinsdóttir, S., Ellis, S., &
404 Wadsworth, F. B. (2021). Volcanic unrest at Taupō volcano in 2019: Causes,
405 mechanisms and implications. *Geochemistry, Geophysics, Geosystems*, 22(6),
406 e2021GC009803. <https://doi.org/10.1029/2021GC009803>
- 407 Iyer, H. M., Gaur, V. K., Rai, S. S., Ramesh, D. S., Rao, C. V. R., Srinagesh, D., &
408 Suryaprakasam, K. (1989). High velocity anomaly beneath the Deccan volcanic
409 province: Evidence from seismic tomography. *Proceedings of the Indian Academy of*
410 *Sciences-Earth and Planetary Sciences*, 98(1), 31-60.
411 <https://doi.org/10.1007/BF02880375>
- 412 Jaxybulatov, K., Shapiro, N. M., Koulakov, I., Mordret, A., Landès, M., & Sens-Schönfelder,
413 C. (2014). A large magmatic sill complex beneath the Toba caldera. *Science*,
414 346(6209), 617-619. <https://doi.org/10.1126/science.1258582>
- 415 Jay, A. E., & Widdowson, M. (2008). Stratigraphy, structure and volcanology of the SE
416 Deccan continental flood basalt province: implications for eruptive extent and
417 volumes. *Journal of the Geological Society*, 165, 177-188.
418 <https://doi.org/10.1144/0016-76492006-062>
- 419 Johnson, J. H., Savage, M. K., & Townend, J. (2011). Distinguishing between stress-induced
420 and structural anisotropy at Mount Ruapehu Volcano, New Zealand. *Journal of*
421 *Geophysical Research: Solid Earth*, 116(B12). <https://doi.org/10.1029/2011JB008308>
- 422 Julia, J., Ammon, C. J., Herrmann, R. B., & Correig, A. M. (2000). Joint inversion of receiver
423 function and surface wave dispersion observations. *Geophysical Journal*
424 *International*, 143(1), 99-112. <https://doi.org/10.1046/j.1365-246x.2000.00217.x>

- 425 Kaila, K. L., Reddy, P. R. Dixit, M. M., & Lazarenko, M. A. (1981). Deep crustal structure at
426 Koyna, Maharashtra, indicated by deep seismic soundings. *Journal of the*
427 *Geological Society of India*, 22 (1) 1-16.
- 428 Kasbohm, J. (2022). Flood basalt buildup warms climate. *Nature Geoscience*, 15(5), 342-
429 343. <https://doi.org/10.1038/s41561-022-00944-z>
- 430 Keir, D., Kendall, J. M., Ebinger, C. J., & Stuart, G. W. (2005). Variations in late syn-rift
431 melt alignment inferred from shear-wave splitting in crustal earthquakes beneath the
432 Ethiopian rift. *Geophysical Research Letters*, 32(23).
433 <https://doi.org/10.1029/2005GL024150>
- 434 Keir, D., Belachew, M., Ebinger, C. J., Kendall, J. M., Hammond, J. O., Stuart, G. W., &
435 Rowland, J. V. (2011). Mapping the evolving strain field during continental breakup
436 from crustal anisotropy in the Afar Depression. *Nature Communications*, 2(1), 1-7.
437 <https://doi.org/10.1038/ncomms1287>
- 438 Kern, H., Popp, T., Gorbatshevich, F., Zharikov, A., Lobanov, K. V., & Smirnov, Y. P. (2001).
439 Pressure and temperature dependence of Vp and Vs in rocks from the superdeep well
440 and from surface analogues at Kola and the nature of velocity anisotropy.
441 *Tectonophysics*, 338(2), 113-134. [https://doi.org/10.1016/S0040-1951\(01\)00128-7](https://doi.org/10.1016/S0040-1951(01)00128-7)
- 442 Kind, R., Ni, J., Zhao, W., Wu, J., Yuan, X., Zhao, L., & Hearn, T. (1996). Evidence from
443 earthquake data for a partially molten crustal layer in southern Tibet. *Science*,
444 274(5293), 1692-1694. <https://doi.org/10.1126/science.274.5293.1692>
- 445 Krishna, V. G., Kaila, K. L., & Reddy, P. R. (1991). Low velocity layers in the subcrustal
446 lithosphere beneath the Deccan Traps region of western India. *Physics of the Earth*
447 *and Planetary Interiors*, 67(3-4), 288-302. [https://doi.org/10.1016/0031-](https://doi.org/10.1016/0031-9201(91)90025-D)
448 [9201\(91\)90025-D](https://doi.org/10.1016/0031-9201(91)90025-D)
- 449 Krishnamurthy, P., Gopalan, K., & Macdougall, J. D. (2000). Olivine compositions in picrite
450 basalts and the Deccan volcanic cycle. *Journal of Petrology*, 41(7), 1057-1069.
451 <https://doi.org/10.1093/petrology/41.7.1057>

- 452 Kumar, M. R., & Mohan, G. (2005). Mantle discontinuities beneath the Deccan volcanic
453 province. *Earth and Planetary Science Letters*, 237(1-2), 252-263.
454 <https://doi.org/10.1016/j.epsl.2005.06.034>
- 455 Lees, J. M. (2007). Seismic tomography of magmatic systems. *Journal of Volcanology and*
456 *Geothermal Research*, 167(1-4), 37-56.
457 <https://doi.org/10.1016/j.jvolgeores.2007.06.008>
- 458 Li, S., Unsworth, M. J., Booker, J. R., Wei, W., Tan, H., & Jones, A. G. (2003). Partial melt
459 or aqueous fluid in the mid-crust of Southern Tibet? Constraints from INDEPTH
460 magnetotelluric data. *Geophysical Journal International*, 153(2), 289-304.
461 <https://doi.org/10.1046/j.1365-246X.2003.01850.x>
- 462 Li, Z., & Peng, Z. (2017). Stress-and structure-induced anisotropy in southern California
463 from two decades of shear wave splitting measurements. *Geophysical Research*
464 *Letters*, 44(19), 9607-9614. <https://doi.org/10.1002/2017GL075163>
- 465 Ligorria, J. P., & Ammon, C. J. (1999). Iterative deconvolution and receiver-function
466 estimation. *Bulletin of the seismological Society of America*, 89(5), 1395-1400.
467 <https://doi.org/10.1785/BSSA0890051395>
- 468 Mahan, K. (2006). Retrograde mica in deep crustal granulites: Implications for crustal
469 seismic anisotropy. *Geophysical Research Letters*, 33(24).
470 <https://doi.org/10.1029/2006GL028130>
- 471 Mahoney, J. J. (1988). Deccan traps. In *Continental flood basalts* (pp. 151-194). Springer,
472 Dordrecht. https://doi.org/10.1007/978-94-015-7805-9_5
- 473 McKenzie, D. P. (1984). The generation and compaction of partially molten rock. *Journal of*
474 *Petrology*, 25(3), 713-765. <https://doi.org/10.1093/petrology/25.3.713>
- 475 Mittal, T., Richards, M. A., & Fendley, I. M. (2021). The magmatic architecture of
476 continental flood basalts I: Observations from the Deccan Traps. *Journal of*
477 *Geophysical Research: Solid Earth*, 126(12), e2021JB021808.
478 <https://doi.org/10.1029/2021JB021807>

- 479 Mohan, G., & Kumar, M. R. (2004). Seismological constraints on the structure and
480 composition of western Deccan volcanic province from converted phases.
481 *Geophysical research letters*, 31(2). <https://doi.org/10.1029/2003GL018920>
- 482 Morgan, W. J. (1972). Deep mantle convection plumes and plate motions. *AAPG bulletin*,
483 56(2), 203-213. <https://doi.org/10.1306/819A3E50-16C5-11D7-8645000102C1865D>
- 484 Moschetti, M. P., Ritzwoller, M. H., Lin, F., & Yang, Y. (2010). Seismic evidence for
485 widespread western-US deep-crustal deformation caused by extension. *Nature*,
486 464(7290), 885-889. <https://doi.org/10.1038/nature08951>
- 487 Muirhead, J. D., Airoidi, G., White, J. D., & Rowland, J. V. (2014). Cracking the lid: Sill-fed
488 dikes are the likely feeders of flood basalt eruptions. *Earth and Planetary Science*
489 *Letters*, 406, 187-197. <https://doi.org/10.1016/j.epsl.2014.08.036>
- 490 Nava, H.A., Black, B. A., Gibson, S. A., Bodnar, R. J., Renne, P. R., & Vanderkluysen, L.
491 (2021). Reconciling early Deccan Traps CO₂ outgassing and pre-KPB global climate.
492 *Proceedings of the National Academy of Sciences*, 118(14), e2007797118.
493 <https://doi.org/10.1073/pnas.2007797118>
- 494 Patro, P. K., & Sarma, S. V. S. (2016). Evidence for an extensive intrusive component of the
495 Deccan Large Igneous Province in the Narmada Son Lineament region, India from
496 three dimensional magnetotelluric studies. *Earth and Planetary Science Letters*, 451,
497 168-176. <https://doi.org/10.1016/j.epsl.2016.07.005>
- 498 Patro, P. K., Raju, K., & Sarma, S. V. S. (2018). Some Insights into the Lithospheric
499 Electrical Structure in the Western Ghat Region from Magnetotelluric Studies.
500 *Journal of the Geological Society of India*, 92(5), 529-532. [https://doi:](https://doi.org/10.1007/s12594-018-1062-z)
501 [10.1007/s12594-018-1062-z](https://doi.org/10.1007/s12594-018-1062-z)
- 502 Paulatto, M., Hooft, E., Chrapkiewicz, K., Heath, B., Toomey, D., & Morgan, J. (2022).
503 Advances in seismic imaging of magma and crystal mush. *Frontiers in Earth Science*,
504 10:970131. <https://doi.org/10.3389/feart.2022.970131>
- 505 Peng, X., & Humphreys, E. D. (1998). Crustal velocity structure across the eastern Snake
506 River Plain and the Yellowstone swell. *Journal of Geophysical Research: Solid*
507 *Earth*, 103(B4), 7171-7186. <https://doi.org/10.1029/97JB03615>

- 508 Prasad, K. N. D., Singh, A. P., & Tiwari, V. M. (2018). 3D upper crustal density structure of
509 the Deccan Syneclise, Central India. *Geophysical Prospecting*, 66(8), 1625-1640.
510 <https://doi.org/10.1111/1365-2478.12675>
- 511 Rai, S. S., Singh, S. K., Sarma, P. V. S. S., Srinagesh, D., Reddy, K. N. S., Prakasam, K. S.,
512 & Satyanarayana, Y. (1999). What triggers Koyna region earthquakes? Preliminary
513 results from seismic tomography digital array. *Proceedings of the Indian Academy of*
514 *Sciences-Earth and Planetary Sciences*, 108(1), 1-14.
515 <https://doi.org/10.1007/BF02840820>
- 516 Ray, L., Gupta, R. K., Chopra, N., Gopinadh, D., & Dwivedi, S. K. (2021). Thermal and
517 physical properties of Deccan basalt and Neoproterozoic basement cores from a deep
518 scientific borehole in the Koyna– Warna seismogenic region, Deccan Volcanic
519 Province, western India: Implications on thermal modeling and seismogenesis. *Earth*
520 *and Space Science*, 8(10), e2021EA001645. <https://doi.org/10.1029/2021EA001645>
- 521 Richards, M. A., Duncan, R. A., & Courtillot, V. E. (1989). Flood basalts and hot-spot tracks:
522 plume heads and tails. *Science*, 246(4926), 103-107.
523 <https://doi.org/10.1126/science.246.4926.103>
- 524 Ridley, V. A., & Richards, M. A. (2010). Deep crustal structure beneath large igneous
525 provinces and the petrologic evolution of flood basalts. *Geochemistry, Geophysics,*
526 *Geosystems*, 11(9). <https://doi.org/10.1029/2009GC002935>
- 527 Saha, G., Rai, S. S., & Shalivahan. (2019). Occurrence of diamond in peninsular India and its
528 relationship with deep Earth seismic properties. *Journal of Earth System Science*, 128,
529 43. <https://doi.org/10.1007/s12040-019-1088-7>
- 530 Saha, G. K., Prakasam, K. S., & Rai, S. S. (2020). Diversity in the peninsular Indian
531 lithosphere revealed from ambient noise and earthquake tomography. *Physics of the*
532 *Earth and Planetary Interiors*, 306, 106523.
533 <https://doi.org/10.1016/j.pepi.2020.106523>
- 534 Savage, B., Covellone, B. M., & Shen, Y. (2017). Wave speed structure of the eastern North
535 American margin. *Earth and Planetary Science Letters*, 459, 394-405.
536 <https://doi.org/10.1016/j.epsl.2016.11.028>

- 537 Self, S., Blake, S., Sharma, K., Widdowson, M., & Sephton, S. (2008). Sulfur and chlorine in
538 Late Cretaceous Deccan magmas and eruptive gas release. *Science*, 319(5870), 1654-
539 1657. <https://doi.org/10.1126/science.1152830>
- 540 Self, S., Mittal, T., Dole, G., & Vanderkluysen, L. (2022). Toward Understanding Deccan
541 Volcanism. *Annual Review of Earth and Planetary Sciences*, 50, 477-506.
542 <https://doi.org/10.1146/annurev-earth-012721-051416>
- 543 Sen, G. (2001). Generation of Deccan trap magmas. *Journal of Earth System Science*, 110(4),
544 409-431. <https://doi.org/10.1007/BF02702904>
- 545 Sen, G., & Chandrasekharam, D. (2011). Deccan Traps Flood Basalt Province: An evaluation
546 of the thermochemical plume model. In *Topics in igneous petrology* (pp. 29-53).
547 Springer, Dordrecht. https://doi.org/10.1007/978-90-481-9600-5_2
- 548 Shapiro, N. M., Ritzwoller, M. H., Molnar, P., & Levin, V. (2004). Thinning and flow of
549 Tibetan crust constrained by seismic anisotropy. *Science*, 305(5681), 233-236.
550 <https://doi.org/10.1126/science.1098276>
- 551 Shapiro, N. M., Campillo, M., Stehly, L., & Ritzwoller, M. H. (2005). High-resolution
552 surface-wave tomography from ambient seismic noise. *Science*, 307(5715), 1615-
553 1618. <https://doi.org/10.1126/science.1108339>
- 554 Sharma, J., Kumar, M. R., Roy, K. S., & Roy, P. N. S. (2018). Seismic imprints of plume-
555 lithosphere interaction beneath the northwestern Deccan Volcanic Province. *Journal*
556 *of Geophysical Research: Solid Earth*, 123(12), 10-831.
557 <https://doi.org/10.1029/2018JB015947>
- 558 Shukla, M. K., Vishnu, C. S., & Roy, S. (2022). Petrographic and geochemical characteristics
559 of the granitic basement rocks below Deccan Traps obtained from scientific drilling to
560 3014 m depth in the Koyna region, western India. *Journal of Earth System Science*,
561 131(2), 1-19. <https://doi.org/10.1007/s12040-022-01888-z>
- 562 Sparks, R. S. J., Huppert, H. E., & Turner, J. S. (1984). The fluid dynamics of evolving
563 magma chambers. *Philosophical Transactions of the Royal Society of London. Series*
564 *A, Mathematical and Physical Sciences*, 310(1514), 511-534.
565 <https://doi.org/10.1098/rsta.1984.0006>

- 566 Takei, Y. (2000). Acoustic properties of partially molten media studied on a simple binary
567 system with a controllable dihedral angle. *Journal of Geophysical Research: Solid*
568 *Earth*, 105(B7), 16665-16682. <https://doi.org/10.1029/2000JB900124>
- 569 Taylor, M. A. J., & Singh, S. C. (2002). Composition and microstructure of magma bodies
570 from effective medium theory. *Geophysical Journal International*, 149(1), 15-21.
571 <https://doi.org/10.1046/j.1365-246X.2002.01577.x>
- 572 Tian, X., & Buck, W. R. (2022). Intrusions induce global warming before continental flood
573 basalt volcanism. *Nature Geoscience*, 15(5), 417-422. [https://doi.org/10.1038/s41561-](https://doi.org/10.1038/s41561-022-00939-w)
574 [022-00939-w](https://doi.org/10.1038/s41561-022-00939-w)
- 575 Tiwari V. M., Rao, M. B. S. V., & Mishra D. C. (2001) Density inhomogeneities under
576 Deccan Volcanic Province as derived from gravity data. *Journal of Geodynamics*,
577 31(1), 1-17. [https://doi.org/10.1016/S0264-3707\(00\)00015-6](https://doi.org/10.1016/S0264-3707(00)00015-6)
- 578 Ward, K. M., Zandt, G., Beck, S. L., Christensen, D. H., & McFarlin, H. (2014). Seismic
579 imaging of the magmatic underpinnings beneath the Altiplano-Puna volcanic complex
580 from the joint inversion of surface wave dispersion and receiver functions. *Earth and*
581 *Planetary Science Letters*, 404, 43-53. <https://doi.org/10.1016/j.epsl.2014.07.022>
- 582 Watanabe, T. (1993). Effects of water and melt on seismic velocities and their application to
583 characterization of seismic reflectors. *Geophysical Research Letters*, 20(24), 2933-
584 2936. <https://doi.org/10.1029/93GL03170>
- 585 Zhai, Y., & Levander, A. (2011). Receiver function imaging in strongly laterally
586 heterogeneous crust: Synthetic modeling of BOLIVAR data. *Earthquake Science*,
587 24(1), 45-54. <https://doi.org/10.1007/s11589-011-0768-4>
- 588 Zheng, T. Y., He, Y. M., Yang, J. H., & Zhao, L. (2015). Seismological constraints on the
589 crustal structures generated by continental rejuvenation in northeastern China.
590 *Scientific Reports*, 5(1), 1-8. <https://doi.org/10.1038/srep14995>
- 591 Zinke, J. C., & Zoback, M. D. (2000). Structure-related and stress-induced shear-wave
592 velocity anisotropy: observations from microearthquakes near the Calaveras Fault in
593 Central California. *Bulletin of the Seismological Society of America*, 90(5), 1305-
594 1312. <https://doi.org/10.1785/0119990099>

- 595 Zhu, L., & Kanamori, H. (2000). Moho depth variation in southern California from
596 teleseismic receiver functions. *Journal of Geophysical Research: Solid Earth*,
597 *105*(B2), 2969-2980. <https://doi.org/10.1029/1999JB900322>
- 598 Zorin, Y. A., Turutanov, E. K., Mordvinova, V. V., Kozhevnikov, V. M., Yanovskaya, T. B.,
599 & Treussov, A. V. (2003). The Baikal rift zone: the effect of mantle plumes on older
600 structure. *Tectonophysics*, *371*(1-4), 153-173. [https://doi.org/10.1016/S0040-](https://doi.org/10.1016/S0040-1951(03)00214-2)
601 [1951\(03\)00214-2](https://doi.org/10.1016/S0040-1951(03)00214-2)